Kinetically Induced Memory Effect in Li-ion Batteries

Pierfrancesco Ombrini[1,†], Qidi Wang[1,†], Alexandros Vasileiadis[1], Fangting Wu[2], Ziyao Gao[2], Xia Hu[2], Martijn van Hulzen[1], Baohua Li[2], Chenglong Zhao[1,*], Marnix Wagemaker[1,*]

[1]Department of Radiation Science and Technology, Delft University of Technology, Delft, 2629JB, the Netherlands.

[2]Shenzhen Key Laboratory on Power Battery Safety and Shenzhen Geim Graphene Center, School of Shenzhen International Graduate School, Tsinghua University, Guangdong, 518055, China.

[†]P.O. and Q.W. contributed equally to this work.

*Corresponding author. Email: c.zhao-1@tudelft.nl; m.wagemaker@tudelft.nl.

Abstract

Effective optimization and control of lithium-ion batteries cannot neglect the relation between fundamental physicochemical phenomena and performance. In this work, we apply a multi-step charging protocol to commercially relevant electrodes, such as $LiNi_{0.8}Mn_{0.1}Co_{0.1}O_2$ (NMC811), $LiFePO_4$ (LFP), $LiMn_{1.5}Ni_{0.5}O_4$ (LMNO), $LiMn_{0.4}Fe_{0.6}PO_4$ (LMFP), $Li_4Ti_5O_{12}$ (LTO) and $Na_3V_2(PO_4)_3$ (NVP), to investigate how the initial rate affects their kinetic response. Remarkably, electrodes undergoing phase separation exhibit a pronounced counter-intuitive memory effect under high-rate operating conditions. Using operando micro-beam X-ray diffraction, the origin is demonstrated to be embedded in the rate-dependent multi-electrode particle dynamics. Developed phase-field electrochemical models capture the ensemble behavior of electrode particles underlying the kinetically induced memory effect, establishing how the thermodynamics of the nanoscale (particle) level affects macroscopic battery behavior under realistic conditions. These results challenge established battery management strategies, opening the doors for improved characterization and optimization of fast-charging protocols, crucial in minimizing aging and heat production while enhancing energy efficiency and benefitting a wide range of battery-powered applications.

Introduction

The pursuit of a sustainable future has propelled lithium-ion batteries (LIBs) into a pivotal role across diverse technological realms[1]. Initially confined to consumer electronics, LIBs have become indispensable in electric vehicles, renewable energy storage, off-grid power systems, and grid stabilization applications. A comprehensive understanding of the chemo-physical behavior is essential to unlock the full potential of LIBs within complex and multi-component systems such as electric vehicles and grid storage.

The concept of 'memory effect' in batteries has gained widespread recognition in the case of Ni-Cd and Ni-metal-hydride systems, where traces of prior cycling are retained, distorting the voltage profile[2–4]. Interestingly, while this phenomenon has been assumed not to affect LIBs, a pivotal study by Sasaki et al.[5] provided first insights that this may not be true. Researchers[5] redefined the memory effect as 'abnormal changes in working voltage' and provided compelling evidence of its occurrence in materials that undergo phase separation within LIBs. Specifically, when a battery is charged to a designated state of charge (SOC), discharged, and then rapidly recharged, a small but distinctive voltage peak emerges in its voltage profile. Path-dependent effects on the voltage of phase-separating materials were also notably described by Katrašnik[6] and Deng[7] who focused on the relation between the open circuit voltage at a given SOC and the previous discharge pulse.

The common denominator in the aforementioned studies is the possibility of explaining the phenomena through the lenses of the complex kinetic behavior of phase-separating active materials. For the active materials that (de)lithiate following a solid-solution path, such as $LiCoO_2$ (LCO) and $LiNi_xCo_yMn_{1-x-y}O_2$ (NMC), Li diffuses inside the particles uniformly such that, when the current is stopped, the concentration inside the particles quickly equilibrates. Thus, the system evolves without substantial intra or inter-particle heterogeneities, relying solely on the particle's size distribution and position with respect to the electrode's depth as a source of heterogeneities. In contrast, $LiFePO_4$ (LFP) and $Li_4Ti_5O_{12}$ (LTO) undergo phase separation during the (de)lithiation process due to their physio-mechanical properties. At a given state of charge, even under equilibrium conditions, these particles exhibit coexisting Li-poor and Li-rich phases. This fundamental difference in reaction behavior, evident in a flat voltage plateau and a voltage hysteresis [8], is intricately linked to inter-particle heterogeneities.

The literature consistently reveals that the applied current does not uniformly distribute among all particles in the electrode; rather, a subset known as active particles carries the bulk of the current while others remain unaffected in terms of (de)lithiation[9–12]. Moreover, the active particle fraction has been established to be proportionate to the applied rate[9,10]. This phenomenon stems from the size-dependent

energy barrier for the nucleation of the (de)lithiated phase, favoring the reaction in nucleated particles[13]. Consequently, the reaction dynamics exhibit rate-dependent behavior, ranging from particle-by-particle lithiation at low rates to collective lithiation at high rates, where the majority of particles are active to sustain the applied current. This dynamic system finds a consistent mathematical description within the regular solution theory framework[14–17], coupled with phase-field modeling, providing a realistic and predictive depiction of the complex dynamics.

Building on this established theory and the acknowledged path dependence overpotential in electrode materials[5,18–21], our study evaluates the influence that applied rate has on subsequent cycling performance, demonstrating the emergence of a kinetically induced memory effect and its impact on the overpotentials and capacities at fast (dis)charge rates. Further, herein, we demonstrate this to be a general phenomenon in electrodes that exhibit a first-order phase transition upon (dis)charge. Implying operando monitoring of individual electrode crystallites we reveal the role of the active particle fraction, while electrochemical phase-field simulations deepen the understanding of the underlying mechanism. We conclude by recognizing the pivotal role of preceding applied rates in shaping the voltage profile, and its importance on SOC estimation and fast-charging protocols optimization in large-scale aleatory systems coupled with LIBs[22].

Results

Memory effect in commercial battery electrode materials

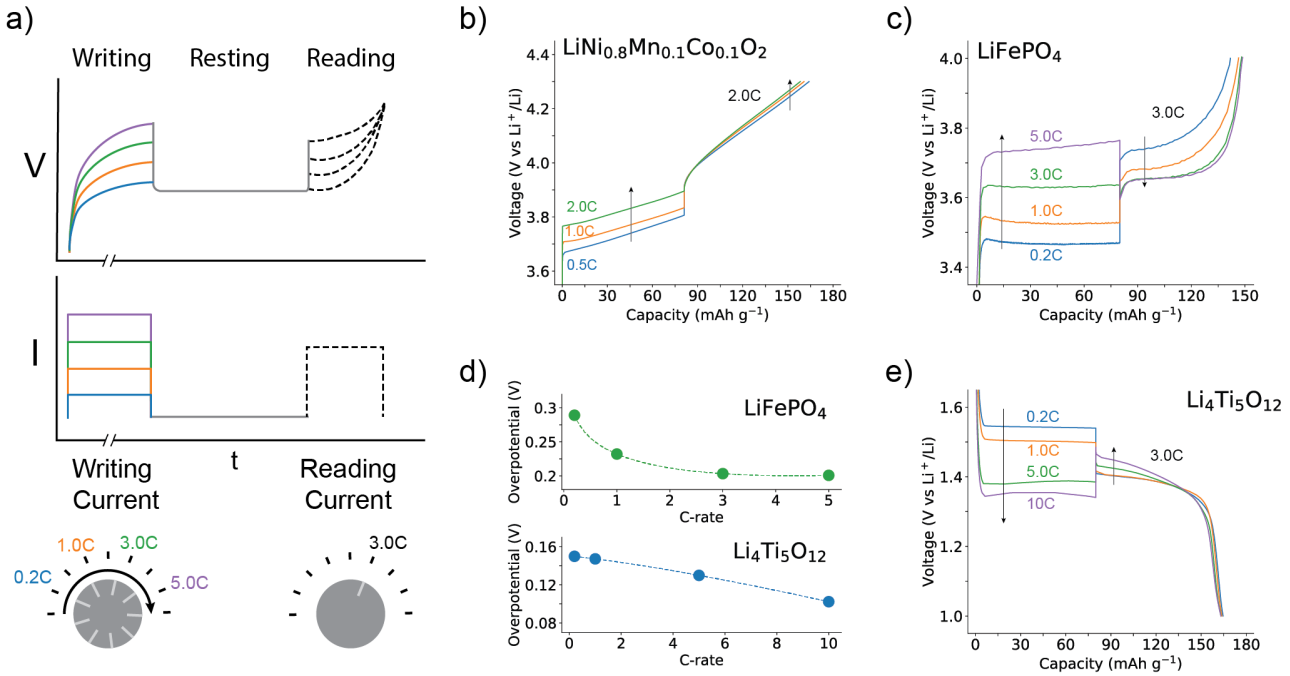

Fig. 1 Demonstration of the kinetically induced memory effects in phase-separating electrode materials. a, Schematic of the memory effect protocol: the depicted colored voltage curves relate to the various currents used in the writing step; zero current is applied during the resting step, and a constant selected current is applied during the reading step. **b**, Voltage profile of NMC811||Li half-cells with the charging rate of 0.5C/1.0C/2.0C in the writing step, 2.0C in the reading step, and the discharge rate of 0.2C (1.0C=180 mA g^{-1}). **c**, Voltage profile of LFP||Li half-cells with the charging rate of 0.2C/1.0C/3.0C/5.0C in the writing step, 3.0C in the reading step, and the discharge rate of 0.2C (1.0C=150 mA g^{-1}). **d**, Overpotentials in LFP||Li and LTO||Li half-cells, measured 60 seconds into the reading step under different rates, where the C-rate refers to the writing step. **e**, Voltage profile of LTO||Li half-cells with the charging rate of 0.2C/1.0C/5.0C/10.0C in the writing step, 3.0C in the reading step, and the charge rate of 0.2C (1.0C=175 mA g^{-1}).

To investigate the effect of the applied rate on the thermodynamic state and consequent dynamic response of battery active materials, we designed a series of (dis)charging protocols (Fig. 1) consisting of three distinct steps: the writing step, the resting step, and the reading step. The writing step refers to a partial (dis)charge of the battery to 50% SOC imposed at varying rates, to induce a non-equilibrium state. Subsequently, a 1-hr resting step under open circuit conditions is applied to let the system

partially relax and ensure no kinetically induced gradients exist. Finally, the reading step completes the (dis)charge process at a fixed rate to examine the impact of the previously imposed rate on the dynamic behavior of the battery. The cell is then slowly cycled towards full charge and discharge before applying the next protocol, bringing the system to an equilibrium state and erasing the effect. Fig. 1a provides a schematic view of the procedure.

The results in Fig. 1b-d illustrate typical electrochemical responses recorded from the described writing, relaxation, and reading steps for commonly used electrode materials. Focusing on the voltage curves during the reading steps, a clear distinction emerges between the different electrode materials. As expected, in the case of $LiNi_{0.8}Co_{0.1}Mn_{0.1}O_2$ (NMC811), in Fig. 1b, when a lower charging rate (0.5C) is applied during the writing step, the reading step shows negligibly lower overpotential compared to writing steps performed at 1.0C or 2.0C. In contrast, the protocol on LFP||Li cell shows a different behavior (Fig. 1c and Fig. S1): when the writing step is conducted at 0.2C, the reading step initiates at 3.75 V, whereas a writing step at 5.0C yields a plateau voltage of 3.63 V. The inverse proportionality between the applied rate and reading step overpotential can be observed clearly in Fig. 1d, where it is also noticeable the presence of a saturation current at 3.0C, above which no reduction in overpotential is present. Moreover, an additional 4% capacity can be charged in the 5.0C-3.0C cycle compared to the 0.2C-3.0C case. This reveals that the overpotential and capacity in the reading steps are influenced by the rate in the writing step, demonstrating that these materials display a kinetically induced memory effect, that is, they are influenced by the previous cycling history. Notably, the LTO||Li cell shows the same unexpected behavior (Fig. 1e) although no saturation current was observed within the range of C-rates tested (Fig. 1d).

The distinguishing factor between LFP, LTO, and NMC is the presence of a first-order phase transition upon (de)lithiation for the first two: materials undergoing a first-order phase separation are susceptible to the kinetically induced memory effect. To confirm this hypothesis, more materials displaying a first-order phase transition, such as $LiNi_{0.5}Mn_{1.5}O_4$ (LMNO), $LiMn_{0.4}Fe_{0.6}PO_4$ (LMFP), and $Na_3V_2(PO_4)_3$ (NVP) were evaluated using similar protocols, also displaying the same phenomenon (Figs. S3-S5). This observation aligns with previously documented memory effects on phase-separating materials[5,6], here demonstrating the great impact on realistic high-rate conditions. Altogether, these results suggest a broad and general phenomenon that highlights the crucial necessity for more extensive investigations into the dynamic response of these materials under diverse operating conditions.

Monitoring the phase transition behavior in individual grains

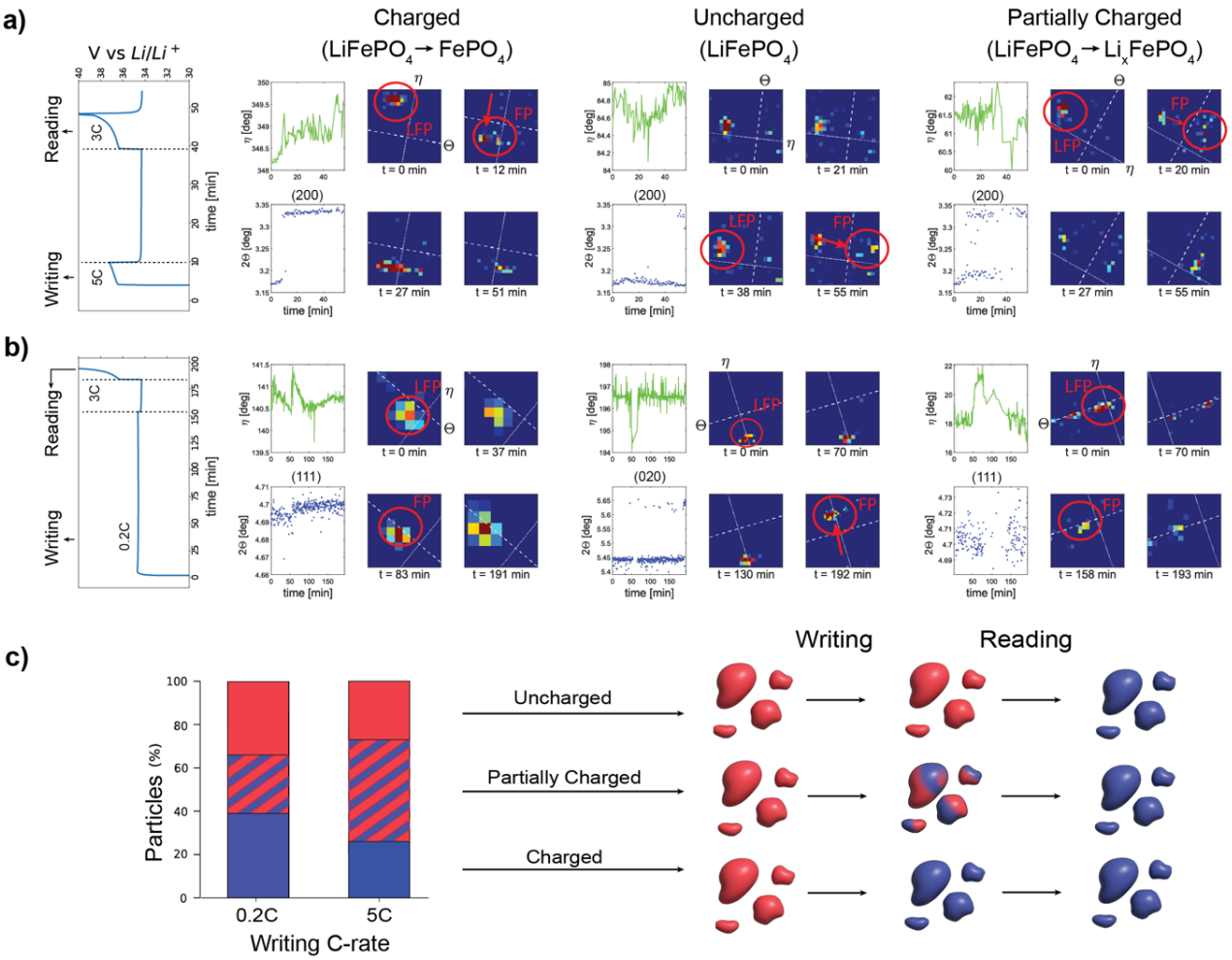

Fig. 2 Microbeam x-ray diffraction analysis. Examples of single-particle diffraction patterns during operation for the cases of **a**, 0.2C writing-3.0C reading and **b**, 5.0C writing-3.0C reading protocols with 30 min rest at 50% SOC. The grains are divided into active in both steps, active solely during the writing and reading steps (first, second, and third columns, respectively). **c**, Summary of the grain evolution during the memory protocol at 0.2C and 5.0C. Percentage of particles charged during the writing step (blue), partially charged (stripes), and discharged (red).

In order to better describe the kinetically induced memory effect, we investigated the impact of applied rates on the active particle population throughout different stages of the test protocol. LFP was selected as the representative material for this study, with the primary objective of quantifying the active particle fraction during variable reading rates. A unique method to monitor the phase transformation of individual crystallites (primary particles) during operando conditions in pouch cells is microbeam X-ray diffraction[10,11].

Two different charging protocols were applied on the same battery: 5C charge, 30 minutes rest, 3C charge, and 0.2C charge, 30 minutes rest and 3C charge, both followed by a 0.1C memory-erasing discharge, thus only differing in the charge rate during the writing step. Approximately 100 reflections, representing an equal amount of $LiFePO_4$ crystallites, were tracked during the electrochemical protocol with the same methodology applied by van Hulzen[10,11]. From hereon we refer to one crystallite as one particle. The anticipated first-order phase transition between $LiFePO_4$ (LFP) and $FePO_4$ (FP) is observed through the disappearance of the LFP reflection and the appearance of the FP reflection at a different 2θ. Particle categorization is established on the observed shift of the 2θ reflections at the conclusion of the writing step. Charged particles are identified based on the exclusive presence of the peak associated with the FP phase; partially charged particles exhibit both the FP and LFP peaks, indicating partial delithiation; uncharged particles retain an unaffected LFP phase and are activated only during the subsequent reading step.

Analyzing the microbeam results provides direct insights into the role of the active particle population in the kinetically induced memory effect under operando conditions. Specifically, under a 0.2C charge rate (writing step), a particle-by-particle lithiation mechanism is observed, with 39% of the particles being charged (full phase transition from LFP to FP) and 27% nucleating the lithium-poor phase without completing the charge (i.e., the coexistence of LFP and FP phases) while the rest remain uncharged (LFP phase). Subsequently, during the 3.0 reading step, the remaining particles (61%) are charged by the imposed current. In contrast, when subjected to a 5.0C rate during the writing step, a more concurrent phase transformation mechanism is observed. In this case, a lower fraction of particles (26%) achieve full charge during this step, while the majority (47%) enter the resting period partially charged, in a phase-separated state. The subsequent 3.0C current can then be sustained by a higher fraction of particles (74%) being either partially charged or uncharged. These findings, summarized graphically in Fig. 2c, underscore the complex relationship between charging rates of the active particle population, shedding light on the dynamics of (de-)lithiation processes within the electrode.

The kinetically induced memory effect can be explained by the difference in multi-particle dynamics during the reading step. Specifically, under high applied rates, the increased active population results in a higher number of nucleated particles at the end of the writing step (50% SOC). Consequently, these nucleated particles become more accessible to the system during the subsequent reading step, having already surmounted the nucleation energy barrier. Notably, these nucleated particles persist during the resting period. Conversely, under low applied writing rates reaches 50% SOC following a mosaic scheme, where the majority of the particles are either uncharged (lithiated) or completely

charged (delithiated). In the subsequent reading step, the need to overcome the nucleation barrier for a larger quantity of particles requires greater overpotentials while the maximum available active particle population is lower. As a consequence, higher potentials are observed throughout the remaining charging process as shown in Fig 1b.

Previous work[10,11] described the formation of a metastable solid solution phase transition in LFP, such that, during a fast (dis)charge, the particle cannot proceed toward phase separation due to the mismatch in characteristic times between reaction and diffusion kinetics. In contrast, no solution phase transition at 5C was observed within this study, which can be attributed to a fundamental distinction in particle shape. Specifically, leveraging the [010] crystalline direction for 1D fast diffusion kinetics, platelet-shaped LFP particles demonstrate a reaction-limited behavior. On the other hand, the spheroidal commercial particles employed in this work (Figs. S7-S9), characterized by higher defect concentrations and, consequently, quasi-isotropic diffusivity, exhibit an effectively diffusion-limited behavior resulting in a more favorable phase separation. Moreover, the presence of the kinetically induced memory effect in a wide set of phase-separating materials (Fig. 1e and Figs. S3-S5) shows that the presence of a metastable solid solution transition in LFP is not a decisive factor in explaining the observed memory effect.

Electrochemical modeling of the memory effect

To further unravel the underlying mechanisms responsible for the kinetically induced memory effect and to gain a deeper understanding of the collective thermodynamic behavior, we implied electrochemical porous electrode models extended to encompass the thermodynamics of phase-separating active particles through phase-field modeling[14]. These models, which naturally account for size-dependent nucleation barriers[23–25], predict the behavior of phase-separating active battery materials at both the single-particle and multi-particle levels under various operating conditions[7,9,15,17,26–32]. As a result, the coupling between phase-field and electrochemical modeling can fit experimental voltage curves[28,33], provide an accurate picture of the active particle population[9] , and generate realistic operando X-ray diffractograms[17].

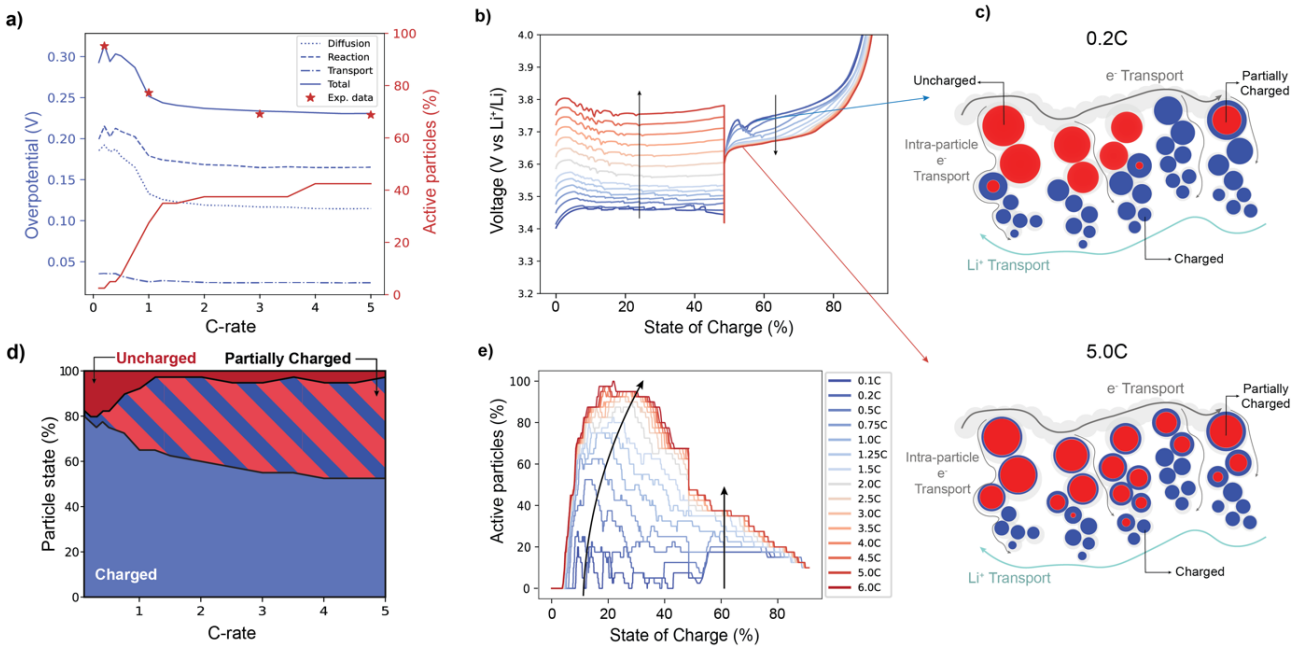

Fig. 3 Electrochemical modeling results. a, Deconvoluted average overpotentials and active particle population at the onset of the reading step vs. writing rate, defined as follows: the reaction overpotential of a single particle is the overpotential driving the reaction, and it corresponds to the difference between the surface chemical potential of the particle and the electrolyte chemical potential at a specific electrode depth; the diffusion overpotential is defined as the difference between the surface chemical potential and the equilibrium potential of the material; the transport overpotential is the difference between the electrochemical potential of Li ions at the Li-metal electrolyte interface and the electrochemical potential at the current collector. The total overpotential is the difference between the equilibrium chemical potential of the LFP plateau and the potential at 55% SOC. **b**, Simulated voltage profiles for the memory protocols of LFP at writing rates varying from 0.1C to 5.0C and fixed reading rate of 3.0C. **c**, Li-ion distribution in a randomly selected ensemble of representative particles of the phase-field simulation at 55% SOC during the reading step for the case of 0.2C and 5.0C writing rates. Blue corresponds to the FP phase, and red corresponds to the LFP phase. **d**, Fraction of particles in the charged, partially charged, and discharged states at 55% SOC at different writing rates. **e**, Evolution of the active particle population during the memory protocols for the simulation presented in b. A particle is considered active if its average lithiation state is between 15% and 85%.

The simulated results for LFP in Fig. 3 unfold the kinetics of the system during the memory protocol, revealing the effect of a range of writing rates on the reading overpotentials. The voltage curves in Fig. 3b are in good agreement with the experimental results (Fig. S10), showing the correct voltage at the onset of the reading steps, the kinetically induced capacity losses, and plateauing at high rates. By analyzing the simulation data, the origin of the total overpotential can separated into its components(Fig. 3a): both the reaction and diffusion overpotentials at the onset of the reading step, are inversely proportional to the applied writing rate, whereas the transport overpotential is marginally affected by the writing rate due the low loading of the tested sample (2 mAh cm^{-2}).

Fig. 3e illustrates the complete multi-particle dynamics by showing the evolution of the active particle population and its corresponding active area during the memory protocol. At low rates, the system maintains a low active particle population during the writing step, following a mosaic lithiation scheme, reaching the reading step with a few phase-separated particles. The system is then forced to overcome the nucleation barrier with a reduced available reactive area. As the writing rate increases, the system reacts more homogenously, accommodating higher currents towards more particles. Due to the wide difference in particle sizes (Figs. S7-S8), the smaller particles will be delithiated faster such that the active particle population starts to decrease before reaching 50% SOC. The kinetic is therefore dominated by the larger-sized particles, which are the system's major current drivers. This imposes a limit on the maximum active particle population achievable during a (dis)charge and explains the saturation of the kinetically induced memory effect at rates higher than 3.0C. After the resting step, where we observe a small drop in active particle fraction due to intra-particle Li exchange (Fig. 3e), the available surface area of the phase-separated particles will accommodate the reading step current.

Fig. 3d depicts the dynamics of the system in the same fashion as described for the micro-beam data: an increase in writing rate leads to a greater fraction of particles being phase-separated at the onset of the reading step. Finally, Fig. 3c visually shows the particle concentration at the beginning of the reading step for the two C-rates explored: 0.2C and 5.0C. The former presents a mosaic lithiation scheme where most particles are found either completely uncharged or charged due to the particle-by-particle lithiation dynamics. In particular, smaller particles are completely charged due to their lower energy barrier for nucleation and faster diffusion times, while bigger particles are mostly uncharged. The 5.0C case is instead mostly composed of phase-separated particles, with only a minority of smaller particles being completely charged.

The thermodynamic interpretation of the phenomenon also clarifies why solid solution materials cannot experience a kinetically induced memory effect. As the electrochemical model demonstrates (Fig. S14), the combination of Fickian diffusion and monotonic chemical potential of solid solution materials impose a fast relaxation of the system: the single particle is rapidly homogenized by internal diffusion, and the difference between the surface concentrations, induced by the previous fast kinetics, drives an inter-particle reaction that quickly homogenizes the system. In phase-separating materials, instead, once the particle is nucleated, both phases will be characterized by similar chemical potentials, and the driving force for multi-particle equilibration is strongly reduced. The origin of this kinetic response is also shown to be general and reproducible in other phase-separating materials as shown by the simulation performed with the $Li_4Ti_5O_{12}$ model[15] (Fig. S13).

Discussion

This study shows and explains a general phenomenon affecting all phase-separating electrode materials: a strong inverse correlation between the initial applied (dis)charging rate and the resulting overpotential during a subsequent step, thus a kinetically induced memory effect. The origin of this behavior is herein described.

Lower rates employed during the writing step of the cycle induce a mosaic lithiation scheme. In this scenario, the reaction primarily occurs for smaller particles, characterized by faster kinetics and a lower energy barrier. Greater overpotentials are instead imposed at higher rates, activating more particles by overcoming size-dependent energy barriers. This results in a larger population of phase-separated particles, delaying their relaxation towards a mosaic scheme due to the coexistence of two phases with the same chemical potential. When the reading current is applied, the former case requires a greater overpotential to activate the single-phase particles and sustain the current with a limited number of available particles. In contrast, the latter case does not require overcoming the nucleation barrier and can evenly distribute the reaction among the majority of particles.

This nuanced interplay between current rates and phase-separation dynamics sheds light on the crucial role of activation barriers and population dynamics in governing the electrochemical behavior of these systems.

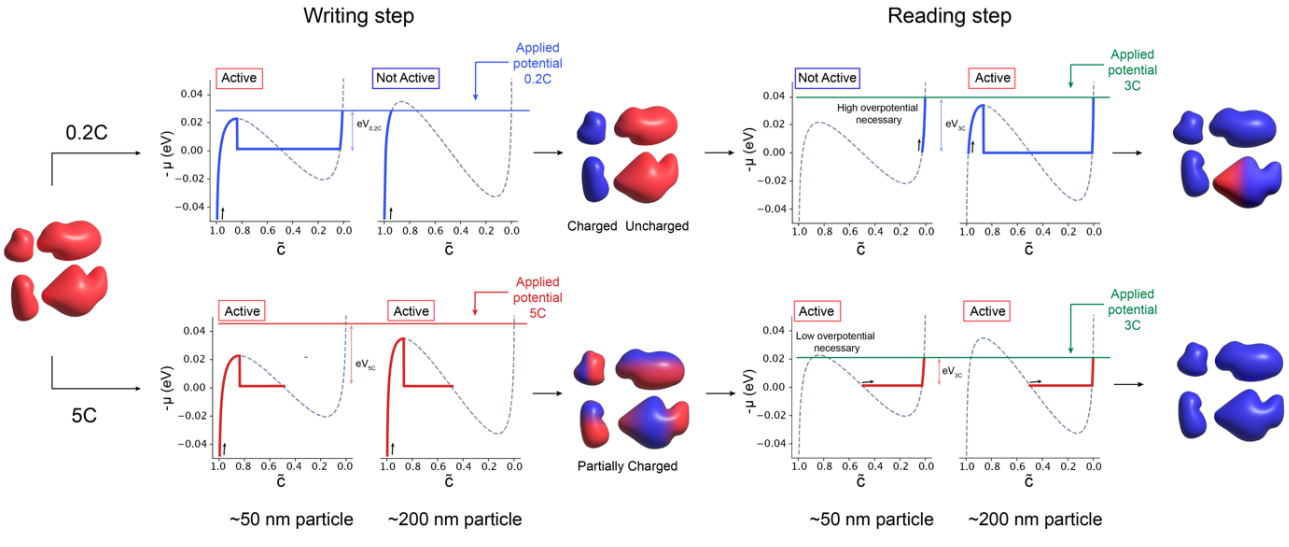

Fig. 4 Schematic summary of the origin of the kinetically induced memory effect. The thermodynamic origin of the memory effect in terms of chemical potential evolution during 0.2C-3C and 5C-3C protocols is described. The size-dependent chemical potentials are calculated based on the approximation of Cogswell et al.[25,34] related to LFP. The represented applied potentials qualitatively show the average overpotential applied to the particle's ensemble during the protocol.

Multiple studies, primarily focusing on LFP, assessed the non-trivial multi-particle and single-particle reaction path that phase-separating materials follow during (de)intercalation[35–39]. Early descriptions relied on a domino-cascade model, suggesting a mosaic particle-by-particle (de)lithiation process[39]. However, subsequent experimental[9,10] and computational[9,15] studies have provided compelling evidence that the active particle population is intricately linked to the applied rate, challenging the initial univocal interpretation. Building on these findings, other works focused on the investigation of the metastable solid solution [23,24,26,27] (characteristic of LFP but not universal to all phase-separating materials) and the relaxation behavior [7,40,41], providing a foundation for the understanding of current-induced phenomena. Specifically, Deng and coworkers[7] characterized the unexpected change in overpotential during quasi-equilibrium discharge of LFP following a high-rate current pulse, revealed by the study of Katrašnik et al.[6], through X-ray microscopy and phase-field modeling on reaction-limited micro-platelet particles. Notably, offering valuable insights, they did not quantitatively assess the strong consequences of these pulses on the subsequent high-rate operating conditions.

Our protocol, closer to commercially relevant rates, reveals the impact of these non-equilibrium phenomena on typical battery operations. The thermodynamic interpretation of it (Fig. 4), obtained by combining modeling and operando monitoring of individual particles, opens the doors to improved protocol design for both deeper fundamental understating and battery management strategies.

For instance, a robust indication of the multi-particle dynamics can be obtained by applying the multi-step protocol: the saturation current (Fig. 1d) offers valuable insights into a possible optimal charging rate able to activate the majority of particles within the electrode (assuming the electrode under study to be the limiting factor); in the case of novel materials, such as LMNO, LMFP and NVP[42], the memory effect becomes a tool for characterizing specific regions of the capacity that exhibit phase separation (Figs. S3-S5).

Moreover, our study underlines the significant implications that may arise from oversimplifying the treatment of phase-separating materials, both computationally and experimentally. Although single-particle models have demonstrated their ability to predict constant current voltage profiles[43], they fall short in capturing behaviors intrinsically linked to the active particle population and phase separation that, as shown here, have a significant effect on the voltage profile prediction and the subsequent management and optimization of battery operations[44–47]. It becomes so critical, when modeling phase-separating materials, to account for multi-particle dynamics and phase-separation kinetics to correctly predict voltage and current responses in complex protocols. Thus, this study proves the necessity of

phase-field methods for improving state-of-the-art battery management strategies[48], since combining multi-step protocols with physically consistent models can maximize the active particle population, directly translating into the reduction of intra-particle stresses, side reactions, heat generation, and energy consumption.

Finally, we show how the continual pursuit of fundamental knowledge in the field of batteries has direct implications on current technology, leading to better protocols for battery management systems, improving battery performance, energy efficiency, and lifespan, ultimately contributing to advancing battery technologies and the broader field of energy storage systems.

Methods

Materials

$LiFePO_4$ was obtained from Leneng Technology for which the cathodes were prepared by mixing $LiFePO_4$ material, poly(vinylidene difluoride) (PVDF, MTI) binder and Super P (Alfa Aesar) conductive carbon in a weight ratio of 92:4:4. The resulting slurry was cast on the Al foil then dried at 60 °C for 6 h, followed by drying overnight at 120 °C in a vacuum oven. $Li_4Ti_5O_{12}$ anode and $LiNi_{0.5}Mn_{1.5}O_4$ were purchased from MTI Corporation and used as received. $LiNi_{0.8}Co_{0.1}Mn_{0.1}O_2$ (NMC811) was synthesized using coprecipitation method: A certain amount of alkaline aqueous solution (NH_4OH and NaOH) was poured into deionized water (1.5 L) to form the base solution in a tank reactor under continuous stirring. Then, a 2 M solution of $NiSO_4{\cdot}6H_2O$, $CoSO_4{\cdot}7H_2O$, and $MnSO_4{\cdot}H_2O$ with a molar ratio of 8:1:1 and an aqueous solution of 5 M NH_4OH and 10 M NaOH were added into the base solution in the tank reactor with a steady rate of 8 mL min^{-1}. The coprecipitation temperature was controlled at 50 ºC, and the pH value was maintained at approximately 11 by NH_4OH with a stirring speed of 500 rpm under nitrogen atmosphere. The coprecipitated $Ni_{0.8}Co_{0.1}Mn_{0.1}(OH)_2$ precursor was prepared, which was subsequently washed by deionized water and ethanol for four times and dried in a vacuum at 120 ºC for 24 h. The apparent and tap density of $Ni_{0.8}Co_{0.1}Mn_{0.1}(OH)_2$ precursors were measured at 1.88 g cm^{-3} and 2.06 g cm^{-3}, respectively. For preparation of NMC811 materials, the as-obtained precursor was mixed with $LiOH{\cdot}H_2O$ at a molar ratio of 1:1.03; then heated to 500 ºC for 5 h and subsequently calcined at 780 ºC for 12 h in oxygen atmosphere. After cooling naturally, the material was immediately placed into an Ar-filled glovebox to prevent being exposed to moisture. The NMC811 electrodes were prepared by mixing active material, Super P and PVDF binder in the mass ratio of 90: 5: 5 in N-methyl-2-pyrrolidone (NMP) solvent and cast on Al foil and then dried at 60 °C for 6 h, followed by drying in a vacuum oven at 120 °C overnight. X-ray diffraction pattern demonstrates the pure phase of this prepared NMC811 material. Battery-grade lithium hexafluorophosphate ($LiPF_6$), ethylene carbonate (EC), diethyl carbonate (DEC), fluoroethylene carbonate (FEC) were purchased from E-Lyte innovations, and subsequently dehydrated using a 4 Å molecular sieve (Sigma-Aldrich).

Electrochemical measurements

Electrochemical cycling tests of all batteries were based on CR2032 coin cells assembled in an Ar-filled glove box (H_2O < 0.1 ppm, O_2 < 0.1 ppm) with Celgard 2500 separators and tested at room temperature, unless stated otherwise. The electrolyte used consisted of 1M $LiPF_6$ in EC/DEC (1:1 in volume) with 5% FEC. 70 µL electrolytes were injected into each coin cell for comparison. All coin cells were tested using multi-channel battery testing systems (Land CT2001A or Lanhe G340A). 15.6 mm diameter lithium metal foils with 250 µm thickness were used as both the working and counter electrodes. Electrochemical cycling performance of the electrodes (12 mm diameter) are all tested with an areal capacity of 2 mAh cm^{-2} with lithium metal foils as counter electrode. All the cells underwent to a formation cycle composed by two 0.1C (0.2 mA cm^{-2}) charge-discharge cycles.

Materials characterization

Morphologies of electrodes were measured on a cold field scanning electron microscope (SEM, HITACH-S4800, SU8010). XRD was performed using a Bruker D8 Advance diffractometer equipped with a Cu Kα radiation source (λ_1 = 1.54060 Å, λ_2 = 1.54439 Å at 40 kV and 40 mA). Rietveld refinement of the XRD was carried out using the General Structure Analysis System software with the EXPGUI software interface. TEM experiments were performed on a STEM (JEM-ARM300F, JEOL) operated at 300 kV with a cold field emission gun and double Cs correctors. The microscope was equipped with Gatan OneView and K2 cameras for image recording. STEM images were taken with an electron dose rate of 50–500 e^- $Å^{-2}$ s^{-1} with an exposure time of several seconds for each image, with a built-in drift correction function in GMS3 using the OneView and K2 camera.

Micro-beam diffraction experiments

For the LFP microbeam diffraction experiment, a similar setup was used as described in van Hulzen et al.[10]. The LFP||Li half-cells were prepared as pouch cells and fixed in a clamp with a conic opening on both sides to allow the X-ray beam to pass through. A monochromatic X-ray beam with wavelength 0.2852 Å (energy 43.47 keV) and spot size of ~1 micron was used to register the diffraction patterns on an Eiger2 X CdTe 4M detector with 2068 x 2162 pixels. To increase the number of grains in Bragg condition the sample was rotated along the z-axis (perpendicular to the beam). For all measurements the total rotation was 5° with a step size of 0.05° and an exposure time of 0.05 seconds, collecting 101 frames in about 6 seconds. To mitigate beam damage four locations were probed by rotation resulting in a time resolution of about 30 seconds per location.

Electrochemical phase-field modeling

The physics-based electrochemical model was developed by expanding on the open-source software MPET[14]. The single particle of LFP was simulated by considering diffusion-limited spherically symmetric one-dimensional particle axis so that the local Li concentration c evolves accordingly to

$$\frac{dc}{dt} = -\nabla \cdot \left(\frac{D}{k_B T} \nabla \mu \right) \ ,$$

where D is the concentration-dependent diffusivity and μ is the phase-field chemical potential. The particle's reaction rate R between the particle of concentration c, and the electrolyte of concentration c_{Li^+} is modeled through the Coupled Ion Electron Transfer Theory[49,50], specifically the electron-coupled ion transfer approximation:

$$R = k_0 \left(1 - \frac{c}{c_{max}}\right) \left(\frac{c_{Li^+}}{1 + e^{\eta_f / k_B T}} - \frac{c/c_{max}}{1 + e^{-\eta_f / k_B T}} \right) \operatorname{erfc} \left(\frac{\frac{\lambda}{k_B T} - \sqrt{\left(\frac{\eta_f}{k_B T}\right)^2 + 1 + \sqrt{\frac{\lambda}{k_B T}}}}{2\sqrt{\frac{\lambda}{k_B T}}} \right)$$

where k_0 is the exchange current density, η_f is the formal overpotential and λ is the reorganization energy for the electron transfer. The electrode is discretized into sub-volumes, each consisting of 8 particles of varying sizes

following the experimental particle size distribution. The electrode-level ionic and electronic losses were modeled implying porous electrode theory[16]. Moreover, wiring losses within the sub-volume are considered, similar to the work of Li et al.[9]. A more detailed description of the model can be found in Supplemental information sections 2.a. Model formulation and 2.b. Model parameters.

Supplemental Information

The Supplemental information includes supplemental results, such as electrochemical experiments on other materials, material characterization, and additional phase-field electrochemical modeling results. Moreover, it contains an extended explanation of the model and its parameters.

Acknowledgments

We acknowledge the support of Shell Global Solutions International B.V.

Author Contributions

M.W. and C.Z. conceived the idea. Q.W. and C.Z. designed the experiments. Q.W. and C.Z. performed the material synthesis, characterization, and electrochemical measurements. Q.W. conducted the microbeam X-ray experiments and analyzed data with P.O. and M.H. P.O. and A.V. developed the electrochemical model and analyzed the data. F.W., Z.G., X.H., and B.L. performed the SEM, TEM, and XRD characterization and electrochemical measurements and analyzed the data with Q.W. and C.Z. Q.W., P.O., A.V., C.Z., and M.W. prepared this manuscript with inputs from all other co-authors. Q.W. and P.O. contributed equally to this work.

Declaration of Interest

The authors declare no competing interests.

References

1. Goodenough, J. B. & Park, K.-S. The Li-Ion Rechargeable Battery: A Perspective. *J. Am. Chem. Soc.* **135**, 1167–1176 (2013).
2. Barnard, R., Crickmore, G. T., Lee, J. A. & Tye, F. L. The cause of residual capacity in nickel oxyhydroxide electrodes. *J Appl Electrochem* **10**, 61–70 (1980).
3. Huggins, R. Mechanism of the memory effect in "Nickel" electrodes. *Solid State Ionics* **177**, 2643–2646 (2006).
4. Sato, Y., Takeuchi, S. & Kobayakawa, K. Cause of the memory effect observed in alkaline secondary batteries using nickel electrode. *Journal of Power Sources* (2001).
5. Sasaki, T., Ukyo, Y. & Novák, P. Memory effect in a lithium-ion battery. *Nature Mater* **12**, 569–575 (2013).
6. Katrašnik, T. *et al.* Entering Voltage Hysteresis in Phase-Separating Materials: Revealing the Electrochemical Signature of the Intraparticle Phase-Separated State. *Advanced Materials* 2210937 (2023) doi:10.1002/adma.202210937.
7. Deng, H. D. *et al.* Beyond Constant Current: Origin of Pulse-Induced Activation in Phase-Transforming Battery Electrodes. *ACS Nano* **18**, 2210–2218 (2024).
8. Dreyer, W. *et al.* The thermodynamic origin of hysteresis in insertion batteries. *Nature Mater* **9**, 448–453 (2010).
9. Li, Y. *et al.* Current-induced transition from particle-by-particle to concurrent intercalation in phase-separating battery electrodes. *Nature Mater* **13**, 1149–1156 (2014).

10. van Hulzen, M., Ooms, F. G. B., Wright, J. P. & Wagemaker, M. Revealing Operando Transformation Dynamics in Individual Li-ion Electrode Crystallites Using X-Ray Microbeam Diffraction. *Front. Energy Res.* **6**, 59 (2018).
11. Zhang, X. *et al.* Direct view on the phase evolution in individual LiFePO4 nanoparticles during Li-ion battery cycling. *Nat Commun* **6**, 8333 (2015).
12. Bai, P. & Tian, G. Statistical kinetics of phase-transforming nanoparticles in LiFePO4 porous electrodes. *Electrochimica Acta* **89**, 644–651 (2013).
13. Cogswell, D. A. & Bazant, M. Z. Size-dependent phase morphologies in LiFePO4 battery particles. *Electrochemistry Communications* **95**, 33–37 (2018).
14. Smith, R. B. & Bazant, M. Z. Multiphase Porous Electrode Theory. *J. Electrochem. Soc.* **164**, E3291–E3310 (2017).
15. Vasileiadis, A. *et al.* Toward Optimal Performance and In-Depth Understanding of Spinel Li $_4$ Ti $_5$ O $_{12}$ Electrodes through Phase Field Modeling. *Adv. Funct. Mater.* **28**, 1705992 (2018).
16. Ferguson, T. R. & Bazant, M. Z. Nonequilibrium Thermodynamics of Porous Electrodes. *J. Electrochem. Soc.* **159**, A1967–A1985 (2012).
17. Ombrini, P., Bazant, M. Z., Wagemaker, M. & Vasileiadis, A. Thermodynamics of multi-sublattice battery active materials: from an extended regular solution theory to a phase-field model of LiMnyFe1-yPO4. *npj Comput Mater* **9**, 148 (2023).
18. Katrašnik, T. *et al.* Entering Voltage Hysteresis in Phase-Separating Materials: Revealing the Electrochemical Signature of the Intraparticle Phase-Separated State. *Advanced Materials* **35**, 2210937 (2023).

19. Guo, X. *et al.* Size-Dependent Memory Effect of the LiFePO 4 Electrode in Li-Ion Batteries. *ACS Appl. Mater. Interfaces* **10**, 41407–41414 (2018).

20. Srinivasan, V. & Newman, J. Existence of Path-Dependence in the LiFePO4 Electrode.

21. Jia, J., Tan, C., Liu, M., Li, D. & Chen, Y. Relaxation-Induced Memory Effect of LiFePO 4 Electrodes in Li-Ion Batteries. *ACS Appl. Mater. Interfaces* **9**, 24561–24567 (2017).

22. Shi, W. *et al.* Influence of memory effect on the state-of-charge estimation of large-format Li-ion batteries based on LiFePO4 cathode. *Journal of Power Sources* **312**, 55–59 (2016).

23. Wagemaker, M., Mulder, F. M. & Van der Ven, A. The Role of Surface and Interface Energy on Phase Stability of Nanosized Insertion Compounds. *Adv. Mater.* **21**, 2703–2709 (2009).

24. Wagemaker, M. *et al.* Dynamic Solubility Limits in Nanosized Olivine LiFePO 4. *J. Am. Chem. Soc.* **133**, 10222–10228 (2011).

25. Cogswell, D. A. & Bazant, M. Z. Theory of Coherent Nucleation in Phase-Separating Nanoparticles. *Nano Lett.* **13**, 3036–3041 (2013).

26. Bai, P., Cogswell, D. A. & Bazant, M. Z. Suppression of Phase Separation in LiFePO 4 Nanoparticles During Battery Discharge. *Nano Lett.* **11**, 4890–4896 (2011).

27. Cogswell, D. A. & Bazant, M. Z. Coherency Strain and the Kinetics of Phase Separation in LiFePO 4 Nanoparticles. *ACS Nano* **6**, 2215–2225 (2012).

28. Galuppini, G. *et al.* Nonlinear identifiability analysis of Multiphase Porous Electrode Theory-based battery models: A Lithium Iron Phosphate case study. *Journal of Power Sources* **573**, 233009 (2023).

29. Koo, B. *et al.* Dynamic surface phases controlling asymmetry of high-rate lithiation and delithiation in phase-separating electrodes. *Energy Environ. Sci.* 10.1039.D3EE00341H (2023) doi:10.1039/D3EE00341H.

30. Bazant, M. *et al. Learning Heterogeneous Reaction Kinetics from X-Ray Movies Pixel-by-Pixel*. https://www.researchsquare.com/article/rs-2320040/v1 (2022) doi:10.21203/rs.3.rs-2320040/v1.

31. Schwietert, T. K. *et al.* Phase-Field Computational Framework for Addressing Challenges in Solid-State Batteries. *PRX Energy* **2**, 033014 (2023).

32. Karanth, P. *et al.* A phase inversion strategy for low-tortuosity and ultrahigh-mass-loading nickel-rich layered oxide electrodes. *Cell Reports Physical Science* 101972 (2024) doi:10.1016/j.xcrp.2024.101972.

33. Zhang, Y. *et al.* Towards better Li metal anodes: Challenges and strategies. *Materials Today* **33**, 56–74 (2020).

34. Ferguson, T. R. & Bazant, M. Z. Phase Transformation Dynamics in Porous Battery Electrodes. *Electrochimica Acta* **146**, 89–97 (2014).

35. Malik, R., Abdellahi, A. & Ceder, G. A Critical Review of the Li Insertion Mechanisms in $LiFePO_4$ Electrodes. *J. Electrochem. Soc.* **160**, A3179–A3197 (2013).

36. Brunetti, G. *et al.* Confirmation of the Domino-Cascade Model by $LiFePO_4$/$FePO_4$ Precession Electron Diffraction. *Chem. Mater.* **23**, 4515–4524 (2011).

37. Chueh, W. C. *et al.* Intercalation Pathway in Many-Particle $LiFePO_4$ Electrode Revealed by Nanoscale State-of-Charge Mapping. *Nano Lett.* **13**, 866–872 (2013).

38. Laffont, L. *et al.* Study of the LiFePO $_4$ /FePO $_4$ Two-Phase System by High-Resolution Electron Energy Loss Spectroscopy. *Chem. Mater.* **18**, 5520–5529 (2006).

39. Delmas, C., Maccario, M., Croguennec, L., Le Cras, F. & Weill, F. Lithium deintercalation in LiFePO4 nanoparticles via a domino-cascade model. *Nature Mater* **7**, 665–671 (2008).

40. Liu, H. *et al.* Capturing metastable structures during high-rate cycling of LiFePO $_4$ nanoparticle electrodes. *Science* **344**, 1252817 (2014).

41. Li, Y. *et al.* Fluid-enhanced surface diffusion controls intraparticle phase transformations. *Nature Mater* **17**, 915–922 (2018).

42. Deng, Y. *et al.* Recent Advances of Mn-Rich LiFe $_{1-y}$ Mn $_y$ PO $_4$ ($0.5 \leqslant y < 1.0$) Cathode Materials for High Energy Density Lithium Ion Batteries. *Adv. Energy Mater.* **7**, 1601958 (2017).

43. Pozzato, G. *et al.* Core-Shell Enhanced Single Particle Model for lithium iron phosphate Batteries: Model Formulation and Analysis of Numerical Solutions. *J. Electrochem. Soc.* **169**, 063510 (2022).

44. Azimi, V., Allam, A. & Onori, S. Extending life of Lithium-ion battery systems by embracing heterogeneities via an optimal control-based active balancing strategy. Preprint at http://arxiv.org/abs/2203.04226 (2022).

45. Galuppini, G. *et al. Efficient Computation of Safe, Fast Charging Protocols for Multiphase Lithium-Ion Batteries: A Lithium Iron Phosphate Case Study*. https://www.ssrn.com/abstract=4392427 (2023) doi:10.2139/ssrn.4392427.

46. Rivera-Barrera, J., Muñoz-Galeano, N. & Sarmiento-Maldonado, H. SoC Estimation for Lithium-ion Batteries: Review and Future Challenges. *Electronics* **6**, 102 (2017).

47. Duan, X. *et al.* Electrochemical Modeling of Fast Charging in Batteries. *Advanced Energy Materials* 2400710 (2024) doi:10.1002/aenm.202400710.

48. Habib, A. K. M. A. *et al.* Lithium-Ion Battery Management System for Electric Vehicles: Constraints, Challenges, and Recommendations. *Batteries* **9**, 152 (2023).

49. Fraggedakis, D. *et al.* Theory of coupled ion-electron transfer kinetics. *Electrochimica Acta* **367**, 137432 (2021).

50. Bazant, M. Z. Unified quantum theory of electrochemical kinetics by coupled ion-electron transfer. *Faraday Discuss.* 10.1039.D3FD00108C (2023) doi:10.1039/D3FD00108C.